# Distributed DAE Modelling of Feeders with High Penetration of Inverter-Based Resources

Freeman Martin, Georgios Tzounas, *IEEE Member*

***Abstract*— This paper develops a continuum-based model for steady-state analysis of distribution feeders with high penetration of inverter-based resources (IBRs). The model is derived from Kirchhoff's laws and describes the spatial evolution of voltage magnitude, phase, and power flows along distribution feeders while representing IBR injections and loads through a composite formulation that combines constant-power, constant-current, and constant-current-density behaviours. Analytical results for the DC limit case reveal a formal analogy with the Euler–Bernoulli beam equation, and AC case studies demonstrate the effect of spatially varying injection and load profiles.**

***Index Terms*— Continuum modelling, active distribution networks, inverter-based resources (IBRs), mechanical analogies.**

## I. Introduction

### A. Motivation

Distribution networks are evolving from passive grids with unidirectional power flows to active networks that integrate a growing number of inverter-based renewable sources, energy storage devices and flexible loads. The growing complexity of these networks poses several challenges to their modelling and analysis. This paper departs from standard lumped-node approaches and investigates the potential of a continuum-based representation of voltage variations and power flows along active distribution feeders that integrate numerous inverter-based resources (IBRs).

### B. Literature Review

The underlying motivation for treating a system of lumped elements as a continuum is the potential to gain insight through simplified analysis. This idea is standard in other fields. For example, matter is composed of discrete particles, yet tracking their individual behaviours in complex mechanical systems is often impractical. Instead, treating matter as a continuous field enables analysis of the macroscale behaviour of structures and fluids [1], such as their elastic/plastic deformation under various loading conditions.

In power systems, the idea of continuum-based modelling is first explored through the so-called electromechanical wave approach [2]–[4]. Therein, synchronous machines were represented as a continuous distribution along transmission lines to capture the propagation of power disturbances. Later works explored variations of the same concept in more general network settings, e.g., see [4]–[6]. However, a key requirement for a continuum abstraction to hold is the presence of a high density of lumped elements, whereas real-world transmission networks typically contain few synchronous machines that are electrically dispersed. This makes it difficult to distribute them without losing critical information [7]. For this reason, the above approach achieved only limited success.

A continuum-based modelling approach is particularly well-suited for modern distribution networks that integrate large amounts of IBRs. In such settings, traditional lumped models may become cumbersome to analyse [8], [9], while detailed data for every device may often not even be available. By treating distribution feeders as a continuous medium, techniques from field theory can be applied to produce insightful approximations of spatially varying voltage profiles. Such studies can become increasingly relevant as modern feeders exhibit strong coupling between bidirectional active power flows and voltage due to high $R/X$ ratios, the proximity of voltage-dependent loads, and the presence of controlled IBRs [10], [11]. Nevertheless, the application of continuum modelling to distribution networks has so far remained limited. Preliminary works have explored its potential for continuum analysis to study voltage collapse [12]. These ideas were further developed to study long feeders and examine how spatial variability in consumption and generation affects voltage deviations as the feeder approaches its loadability limit [13]. Moreover, [14] incorporates IBR voltage–reactive power ($v$ - $Q$) controllers into a continuum formulation to analyse voltage stability in long PV-rich feeders. Finally, the behaviour of spatially distributed electric vehicle (EV) charging stations, including the impact of different charging/discharging power injection profiles on feeder voltage profiles, is discussed in [15], [16]. However, these works assume a constant power model for loads and generators, ignoring composite behaviours such as voltage- or current-dependent sources. Furthermore, the uncertainty and stochastic nature of DER-rich systems were not accounted for.

### C. Contribution

This paper develops a continuum model for steady-state analysis of distribution feeders with high penetration of IBRs. Unlike prior works, the proposed model incorporates a composite injection scheme that unifies constant power, constant current, and constant current density. This formulation supports the spatial representation of local control actions, such as voltage–reactive power and power factor regulation within the injection model. It provides analytical insight through a DC limit that exhibits a formal analogy with a beam from mechanics. The resulting model offers a framework for deterministic and stochastic studies of feeders under variable generation and loads, as demonstrated through case studies of cloud-induced disturbances, control strategies, and probabilistic management.

### D. Organization

The remainder of this paper is organised as follows. Section II introduces the continuum model formulation, deriving the governing equations, injection model, and discussing its numerical solution. Section III presents analytical insights, including the DC feeder special case and its mechanical analogy. Numerical simulation results for AC feeders are presented in Section IV. Finally, conclusions are drawn and future work is outlined in Section V.

## II. Continuum Model Formulation

### A. Governing Equations

We consider a distribution feeder with IBRs and loads connected along its length. We examine a small segment between positions $x$ and $x+\Delta x$, as shown in Fig. 1, where $\Delta x$ represents the distance between injection nodes aggregating connected IBRs and loads. The series impedance of the segment is denoted as $\Delta\bar{Z}$. The voltage phasors at the endpoints of the segment are denoted as $\bar{v}(x)$, $\bar{v}(x+\Delta x)$ and the current phasors as $\bar{\imath}(x)$, $\bar{\imath}(x+\Delta x)$. Applying Kirchhoff's laws, the changes in current and voltage across the segment are:

$$\bar{\imath}(x+\Delta x) - \bar{\imath}(x) = \Delta\bar{\imath}(x) \tag{1}$$
$$\bar{v}(x+\Delta x) - \bar{v}(x) = -\Delta\bar{Z}\,[\bar{\imath}(x) + \Delta\bar{\imath}(x)] \tag{2}$$

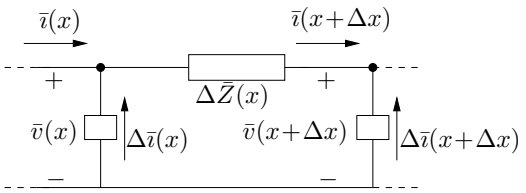


Fig. 1: Segment of active distribution feeder.

By dividing (1), (2) by $\Delta x$ and taking the limit of infinitesimal IBR spacing, we obtain the continuum model:

$$d\bar{\imath}(x)/dx = \bar{J}(x) \tag{3}$$
$$d\bar{v}(x)/dx = -\bar{z}\;\bar{\imath}(x) \tag{4}$$

where $\bar{z} = d\bar{Z}/dx$ is the per-unit-length series impedance at $x$; and $\bar{J}(x)$ is the net current injection density, where:

$$\bar{J}(x) = \bar{J}_G(x) - \bar{J}_D(x)$$

with $\bar{J}_G(x)$ and $\bar{J}_D(x)$ being, respectively, the current densities of power generation and consumption at $x$.

### B. Variation of Voltage Magnitude and Phase

The voltage phasor at $x$ is expressed as $\bar{v} = v\angle\theta$, where $v = v(x)$ and $\theta = \theta(x)$ are the voltage magnitude and phase angle, respectively; and the current phasor as $\bar{\imath} = \imath_P + \jmath\imath_Q$, where $\imath_P = \imath_P(x)$ and $\imath_Q = \imath_Q(x)$ are the active and reactive components of the current, respectively; and $\imath = (\imath_P^2 + \imath_Q^2)^{1/2}$. Substituting into (4), we obtain:

$$e^{\jmath\theta}\left(\frac{dv}{dx} + \jmath v\frac{d\theta}{dx}\right) = -(r\imath_P - \chi\imath_Q) - \jmath(\chi\imath_P + r\imath_Q) \tag{5}$$

where $r$ and $\chi$ are the resistance and reactance per unit length, with $\bar{z} = r + \jmath\chi$. Separating real and imaginary parts in (5):

$$dv/dx = -(r\imath_P - \chi\imath_Q)\cos\theta - (\chi\imath_P + r\imath_Q)\sin\theta \tag{6}$$
$$d\theta/dx = [(r\imath_P - \chi\imath_Q)\sin\theta - (\chi\imath_P + r\imath_Q)\cos\theta]/v \tag{7}$$

where the explicit dependence on $x$ is omitted for brevity. To further simplify (6)-(7), we transform the current components into a rotated frame where one component is aligned with the line impedance and the other is orthogonal to it [17]:

$$\imath_p = (r\imath_P - \chi\imath_Q)/z \tag{8}$$
$$\imath_q = (\chi\imath_P + r\imath_Q)/z \tag{9}$$

where $z = \sqrt{r^2+\chi^2}$. In matrix form:

$$\begin{bmatrix}\imath_p\\ \imath_q\end{bmatrix} = \begin{bmatrix}r/z & -\chi/z\\ \chi/z & r/z\end{bmatrix}\begin{bmatrix}\imath_P\\ \imath_Q\end{bmatrix} = \begin{bmatrix}\cos\beta & -\sin\beta\\ \sin\beta & \cos\beta\end{bmatrix}\begin{bmatrix}\imath_P\\ \imath_Q\end{bmatrix} \tag{10}$$

where $\beta = \arctan(\chi/r)$. Substituting (8)-(9) into (6)-(7), we obtain the following expressions for the spatial evolution of voltage magnitude and phase across the distribution feeder:

$$dv/dx = E \tag{11}$$
$$d\theta/dx = (z\imath_p\sin\theta - z\imath_q\cos\theta)/v \tag{12}$$

where

$$sE = -z\imath_p\cos\theta - z\imath_q\sin\theta \tag{13}$$

### C. Variation of Active and Reactive Power

Let us express the complex power flow $\bar{S}(x)$ at $x$ as follows:

$$\bar{S}(x) = \bar{v}(x)\bar{\imath}^*(x) = P(x) + \jmath Q(x) \tag{14}$$

where $*$ is the complex conjugate. Differentiating with respect to $x$ gives:

$$d\bar{S}/dx = \bar{\imath}^*\;d\bar{v}/dx + \bar{v}\;d\bar{\imath}^*/dx = -\bar{z}\imath^2 + \bar{v}\bar{J}^* \tag{15}$$

In (15), the first term, $-\bar{z}\imath^2$, represents the variation of power flow due to the series impedance, while the second term, $\bar{v}\bar{J}^*$, accounts for the contribution from the power injection of IBRs and loads at $x$. The second term can be written as:

$$\bar{v}\bar{J}^* = dP^{\mathrm{inj}}/dx + \jmath dQ^{\mathrm{inj}}/dx \tag{16}$$

with

$$\begin{aligned} dP^{\mathrm{inj}}/dx &= vJ_P\cos\theta + vJ_Q\sin\theta\\ dQ^{\mathrm{inj}}/dx &= vJ_Q\cos\theta - vJ_P\sin\theta\end{aligned} \tag{17}$$

where $\bar{J} = J_P + \jmath J_Q$.

### D. Distributed Current Density Model

We introduce a composite model for IBRs and loads that combines constant power density, constant current, and constant current density behaviours. Accordingly, the active and reactive current injection densities at $x$ are defined as:

$$J_P = J_{P\mathrm{P}} + J_{P\mathrm{I}} + J_{P\mathrm{J}} \tag{18}$$
$$J_Q = J_{Q\mathrm{P}} + J_{Q\mathrm{I}} + J_{Q\mathrm{J}} \tag{19}$$

Splitting the real and imaginary parts in (3), we obtain:

$$d\imath_P/dx = J_P \tag{20}$$
$$d\imath_Q/dx = J_Q \tag{21}$$

From the solution of (17), $J_P$ and $J_Q$ can be written as:

$$\begin{aligned} J_P &= [(dP^{\text{inj}}/dx)\cos\theta + (dQ^{\text{inj}}/dx)\sin\theta]/v \\ J_Q &= [(dQ^{\text{inj}}/dx)\cos\theta - (dP^{\text{inj}}/dx)\sin\theta]/v \end{aligned} \tag{22}$$

In the following, we describe the expression of each component in (18)-(19).

*1) Constant Power Density:* For a constant power injection density model, we have $dP^{\text{inj}}(x)/dx = P_{d\text{P}} = \text{const.}$ and $dQ^{\text{inj}}(x)/dx = Q_{d\text{P}} = \text{const.}$ Using (22), the expressions of $J_{P\text{P}}$ and $J_{Q\text{P}}$ in (18)-(19) are:

$$J_{P\text{P}} = (P_{d\text{P}}\cos\theta + Q_{d\text{P}}\sin\theta)/v \tag{23}$$
$$J_{Q\text{P}} = (Q_{d\text{P}}\cos\theta - P_{d\text{P}}\sin\theta)/v \tag{24}$$

*2) Constant Current:* For a constant current model, the active and reactive power injections vary linearly with voltage magnitude. Thus, $dP^{\text{inj}}/dx = P_{\text{I}}^{\text{inj}} dv/dx$ and $dQ^{\text{inj}}/dx = Q_{\text{I}}^{\text{inj}} dv/dx$, where $P_{\text{I}}^{\text{inj}}$ and $Q_{\text{I}}^{\text{inj}}$ are constant coefficients. The expressions of $J_{P\text{I}}$ and $J_{Q\text{I}}$ in (18)-(19) are:

$$J_{P\text{I}} = (P_{\text{I}}^{\text{inj}} E\cos\theta + Q_{\text{I}}^{\text{inj}} E\sin\theta)/v \tag{25}$$
$$J_{Q\text{I}} = (Q_{\text{I}}^{\text{inj}} E\cos\theta - P_{\text{I}}^{\text{inj}} E\sin\theta)/v \tag{26}$$

*3) Constant Current Density:* In the constant current density model, the injection profiles $J_{P\text{J}}$ and $J_{Q\text{J}}$ in (18)-(19) are given directly as voltage-independent functions of $x$:

$$J_{P\text{J}} = J_{P\text{J}}(x)\,, \qquad J_{Q\text{J}} = J_{Q\text{J}}(x) \tag{27}$$

We will refer to (18)-(19) as the JIP model.

### *E. Complete Model and Numerical Solution*

Combining the above expressions yields a differential-algebraic system with four state variables and nine algebraic variables. The column vectors of state variables ($\mathbf{x}$) and algebraic variables ($\mathbf{y}$) are defined as:

$$\mathbf{x} = [\imath_P\ \imath_Q\ v\ \theta]^\intercal,\ \mathbf{y} = [\imath_p\ \imath_q\ E\ J_P\ J_Q\ J_{P\text{P}}\ J_{Q\text{P}}\ J_{P\text{I}}\ J_{Q\text{I}}]^\intercal$$

The differential equations are (20), (21), (11), (12). The corresponding algebraic constraints are (8), (9), (13), (18), (19), (23), (24), (25), (26). In total, the system contains 13 variables and 13 equations. The model is a DAE with four differential states and nine algebraic variables. The system uses algebraic relations that are linear and invertible for $v(x) > 0$, and hence is of index 1. Note that the model is non-autonomous, and it becomes autonomous only if all parameters are assumed to be constant along the feeder, that is, only if the feeder is assumed *homogeneous*. The model variables and parameters are summarized in Table I.

The solution of the continuum model constitutes a boundary value problem (BVP) and requires the specification of appropriate boundary conditions. In our case, well-posedness requires four independent boundary conditions, corresponding to the order of the model. As an example, let us consider the case where the voltage magnitude and angle are fixed at one end of the feeder ($x = 0$), while the other end ($x = L$, where $L$ is the line length) is open. The corresponding boundary conditions are:

$$v(0) = v_0\ ,\ \theta(0) = \theta_0\ ,\ \imath_P(L) = 0\ ,\ \imath_Q(L) = 0$$

The boundary values for the algebraic variables are:

$$\begin{aligned} &\imath_p(L)=0\,,\ \imath_q(L)=0\,,\ E(L)=0\,,\ J_P(L)=0, J_Q(L)=0, \\ &J_{P\text{I}}(L)=0\,,\ J_{Q\text{I}}(L)=0\,, \\ &J_{P\text{P}}(0) = [P_{d\text{P}}(0)\cos\theta_0 + Q_{d\text{P}}(0)\sin\theta_0]/v_0 \\ &J_{Q\text{P}}(0) = [Q_{d\text{P}}(0)\cos\theta_0 - P_{d\text{P}}(0)\sin\theta_0]/v_0 \end{aligned}$$

To solve the BVP, one can employ a shooting method [18]. This approach transforms the problem into an equivalent initial value problem, which is numerically more tractable. The idea is to use the known initial values at $x = 0$, guess the remaining ones, and numerically integrate the system forward up to $x = L$. The result is then compared against the desired terminal conditions, and the process is repeated iteratively until convergence is achieved. Each integration from $x = 0$ to $L$ is performed in this paper using the trapezoidal method, while the iterative update of initial conditions is carried out using Newton's method.

Consider the case discussed above, where $v(0)$, $\theta(0)$ are known and $\imath_P(0)$, $\imath_Q(0)$ are unknown. Let $\imath_P^{[k]}(0)$ and $\imath_Q^{[k]}(0)$ denote the guesses at the $k$-th iteration of the process. After integrating the system, we obtain terminal values $\imath_P^{[k]}(L)$ and $\imath_Q^{[k]}(L)$, which are compared to the desired values $\imath_P(L) = 0$ and $\imath_Q(L) = 0$. The corresponding shooting error is:

$$\boldsymbol{\epsilon}^{[k]} = \begin{bmatrix} \imath_P^{[k]}(L) - \imath_P(L) \\ \imath_Q^{[k]}(L) - \imath_Q(L) \end{bmatrix}$$

The initial values are then refined as follows:

$$\begin{bmatrix} \imath_P^{[k+1]}(0) \\ \imath_Q^{[k+1]}(0) \end{bmatrix} = \begin{bmatrix} \imath_P^{[k]}(0) \\ \imath_Q^{[k]}(0) \end{bmatrix} - (\mathbf{J}^{[k]})^{-1}\boldsymbol{\epsilon}^{[k]}$$

where $\mathbf{J}^{[k]}$ is the Jacobian matrix of the shooting error with respect to the initial conditions:

$$\mathbf{J}^{[k]} = \begin{bmatrix} \partial\imath_P^{[k]}(L)/\partial\imath_P^{[k]}(0) & \partial\imath_P^{[k]}(L)/\partial\imath_Q^{[k]}(0) \\ \partial\imath_Q^{[k]}(L)/\partial\imath_P^{[k]}(0) & \partial\imath_Q^{[k]}(L)/\partial\imath_Q^{[k]}(0) \end{bmatrix}$$

TABLE I: Continuum model: variables and parameters.

| Type | List | Total number |
|---|---|---|
| State variables | $\imath_P$, $\imath_Q$, $v$, $\theta$ | 4 |
| Algebraic variables | $\imath_p$, $\imath_q$, $E$, $J_P$, $J_Q$, $J_{P\text{P}}$, $J_{Q\text{P}}$, $J_{P\text{I}}$, $J_{Q\text{I}}$, | 9 |
| Parameters | $r$, $\chi$, $P_{d\text{P}}$, $Q_{d\text{P}}$, $P_{\text{I}}^{\text{inj}}$, $Q_{\text{I}}^{\text{inj}}$, $J_{P\text{J}}$, $J_{Q\text{J}}$ | 8 |

## III. Analytical Results

### *A. Mechanical Analogy of DC Feeder*

Using the notation $v = d\psi/dx$, (4) can be written as:

$$d^3\psi/dx^3 = -rJ_P \tag{28}$$

and thus:

$$d^4\psi/dx^4 = -rdJ_P/dx \tag{29}$$

Note the straight analogy of the last equation with the Euler–Bernoulli Beam Equation [19]:

$$d^4y/dx^4 = f/(\mathcal{E}I) \tag{30}$$

where $\mathcal{E}I$ is the beam flexural rigidity; $y$ is the vertical displacement; and $f$ is the distributed force applied to the beam. The analogy is summarized in Table II.

TABLE II: Analogy of DC feeder with mechanical beam.

| Electrical quantity | Mechanical quantity |
|---|---|
| Voltage integral $\psi(x)$ | Vertical displacement $y(x)$ |
| Voltage $v(x)$ | Deflection angle $\alpha(x)$ |
| Line current $\imath_P(x)$ | Bending moment $M(x)$ |
| Current density $J_P(x)$ | Shear force $F(x) = \mathcal{E}Id^3y(x)/dx^3$ |
| $dJ_P(x)/dx$ | Distributed force $f(x) = dF(x)/dx$ |
| Conductance per unit length $1/r$ | Flexural rigidity $\mathcal{E}I$ |

For the sake of illustration, assume that the DC line has a linearly varying current density, that is $J_P = J_{PJ}$. This case is formally analogous to a beam with uniform distributed force $f$. This analogy can be extended to an AC system by using two rotating disks attached together by an elastic bar.

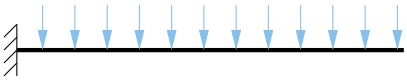

Fig. 2: A cantilever beam with uniform distributed force is analogous to DC feeder with linearly varying current density.

### B. Analytical Results for a DC Feeder

The boundary conditions discussed in Section II-E are applied. As this is a simple case study an analytical expression can be derived. Integrating (3), and taking into account that $\bar{J}(x) = \bar{J}$ is constant, we get:

$$\int_x^L d\bar{\imath} = \int_x^L \bar{J}(l)dl \;\Rightarrow \bar{\imath}(x) = \bar{J}(L-x) = \bar{J}L - \bar{J}x \tag{31}$$

Integrating (4) with respect to $x$, we get:

$$\int_0^x d\bar{v} = -\int_0^x \bar{z}\,\bar{\imath}(l)dl \Rightarrow \bar{v}(x) = \bar{v}_0 - \bar{z}\bar{J}Lx + \frac{\bar{z}\bar{J}}{2}x^2 \tag{32}$$

## IV. Numerical Simulations

As shown in Fig. 3a, the active current injections are constant along the line. This produces a concave-upward voltage profile, the voltage decreases quadratically along the length of the feeder. This result matches the form of the analytically derived voltage equation (32).

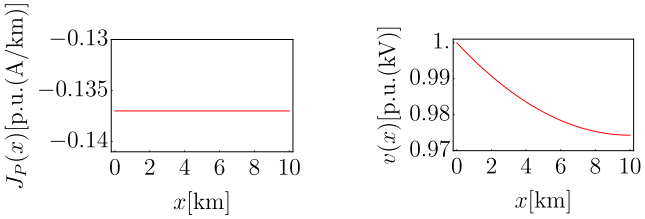


(a) Current injection profile (b) Voltage profile

Fig. 3: DC feeder under constant current injection.

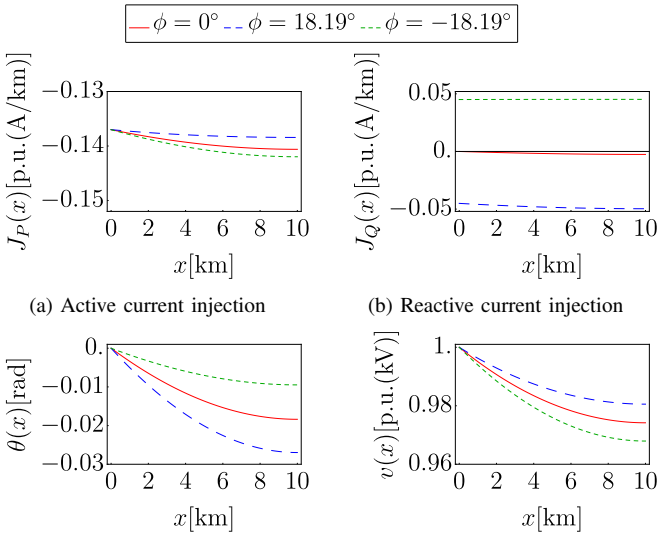


(a) Active current injection (b) Reactive current injection

(c) Voltage angle (d) Voltage magnitude

Fig. 4: AC feeder voltage under different injection phase angles.

### A. AC Feeder

*1) Power factor variation:* The same system can be extended to an AC feeder with a constant power load model. The phase angle of the current injections $\phi$ is varied such that $\phi = \arctan(J_Q/J_P) \in \{0°, 18.19°, -18.19°\}$, in order to compare the behaviour of active, reactive, and complex current injections.

The results in Figs. 4c and 4d highlight the effect of the different injection profiles shown in Fig. 4a and 4b. When $\phi = 0°$, the active power loads decrease the voltage magnitude and phase. For $\phi = 18.19°$, the reactive load components, results in the largest decrease in the voltage phase and the smallest decrease in the voltage magnitude. Finally, when $\phi = -18.19°$ the reactive injections cause the smallest decrease in voltage phase and the greatest decrease in voltage magnitude, this is due to the coupling between the injection terms and angle dynamics causing a greater active power load along the line.

*2) JIP Modelling:* Now, the effects of different load models are examined, constant power $J_{PP}$ and constant current $J_{PI}$. Specifically, 3 scenarios are examined, using purely constant power, purely constant current, and a composite model that uses an equal linear combination of both. The objective is to understand the effects different load models have on the system. The line is uniformly loaded with an area of lighter loading added to the middle of the feeder.

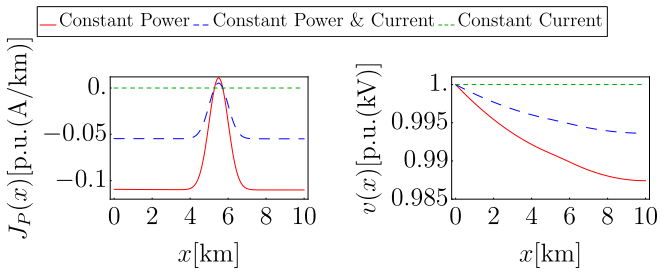


(a) Active current injection profile (b) Voltage magnitude

Fig. 5: AC feeder: Impact of load modeling.

The current injection profiles in Fig. 5a show the differences between the load models. The constant power model results in a significant contribution from the active and reactive load components along the line. This reflects the sensitivity of this model to local voltage variations. In contrast, the constant current model exhibits negligible injections along the line. This behaviour is expected given the equations depend on the spatial voltage gradient, which remains small under typical operating conditions. Consequently, the composite model is dominated by the constant power component.

The voltage magnitude and phase for the constant current model remains unchanged across the length of the feeder, as expected. In the composite and constant power models the voltage magnitude and phase decreases along the feeder indicating the line has a net inductive effect.

*3) Cloud:* Next, a temporal disturbance is examined by introducing a parameter $t$. The temporal disturbance is introduced to emulate the effects of a cloud passing over an area of high PV density. This injection profile is modelled using a Gaussian that is parametrised with respect to $t$.

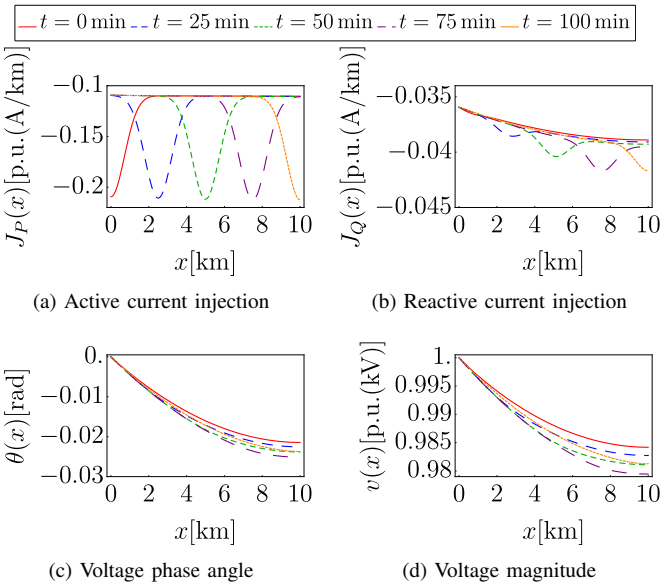


(a) Active current injection (b) Reactive current injection

(c) Voltage phase angle (d) Voltage magnitude

Fig. 6: Impact of moving cloud on the voltage along a PV-rich feeder.

The resulting injection profiles are shown in Figs. 6a and 6b. Despite not directly impacting the reactive injections the disturbance still induces small changes in the reactive load components. The voltage responses are shown in Fig. 6d and 6c. The voltage magnitude and phase exhibited localised variations corresponding to the spatial location of the disturbance. These results demonstrate the model's ability to capture spatially and temporally varying behaviours from intermittent IBR output, such as PV fluctuations due to moving clouds.

*4) Cloud with voltage control scheme:* A similar case using a cloud but with a net active power injection is examined. The control laws used are static, local maps applied per-$x$ without delays. The objective is to illustrate how $\bar{J}(x)$ represents device behaviour in space. A full dynamic and stability analysis is left to future work. A reactive current control scheme is applied which aims to regulate $v(x) = 1$ pu, such that $Q_{dP} = q_0 \tanh\left[(2(v(x) - 1))/\delta\right]$, where $q_0$ defines the magnitude of the controller response, and $\delta$ defines the steepness of the control curve. Applying this new condition to the system and comparing it to the uncontrolled results, we see that the maximum deviations in voltage magnitude are significantly reduced. This demonstrates the effectiveness of reactive current control in stabilising voltages under cloud-induced disturbances.

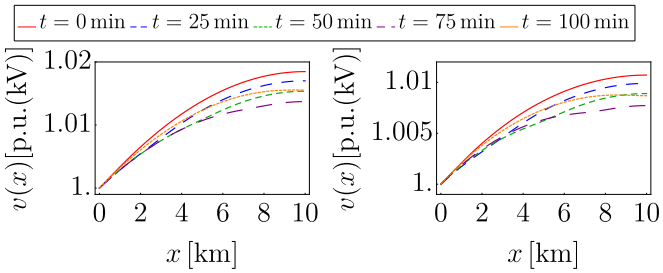


(a) Voltage magnitude, with no control (b) Voltage magnitude, with control

Fig. 7: Impact of control schemes on the voltage along a PV-rich feeder with a moving cloud.

*5) Cloud with power factor control:* A power factor (PF) control scheme is applied to the same scenario, using a target of PF $= 0.9$. The controller computes the desired reactive power density based on the local active power and the reference power factor, such that $Q_{dP} = q_0 \tanh[(P_{dP} \tan(\theta_{\text{ref}}))/q_0]$. By dynamically adjusting the reactive injections the power factor can be pulled towards the reference angle improving over the static reactive injections, especially where the disturbance is applied. This highlights the risk to the DERs pose to power factor fluctuations and demonstrates the capability of power factor controls can improve stability under variable generation conditions.

*6) Stochastic Cloud with Monte Carlo:* Due to the stochastic nature of the weather, the cloud can be modelled using mean reverting stochastic differential equations, specifically a Ornstein–Uhlenbeck process for amplitude, speed, and width, combined with an exponential life time and fade-out factors.

$$P_{dP}(x,t) = P_0(x) - \tilde{A}(t)\,\exp\Big(-\tfrac{(x-\Upsilon(t))^2}{2W^2(t)}\Big)$$

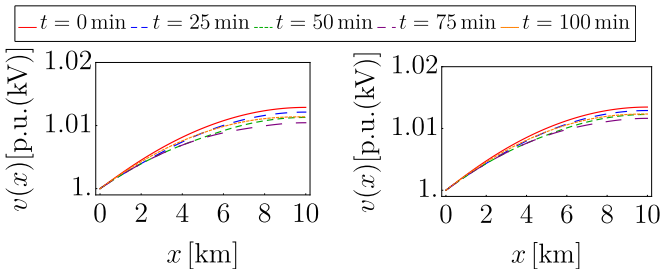


(a) Voltage magnitude, with no control (b) Voltage magnitude, with control

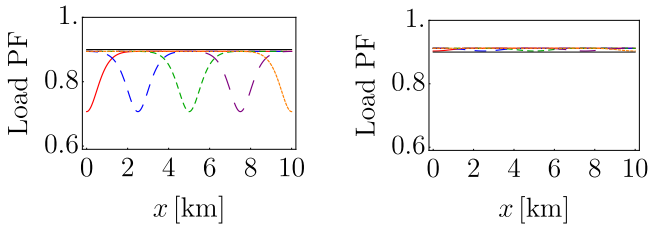


(c) Load power factor, with no control (d) Load power factor, with control

Fig. 8: Impact of power factor control on voltage along PV-rich feeder with a moving cloud.

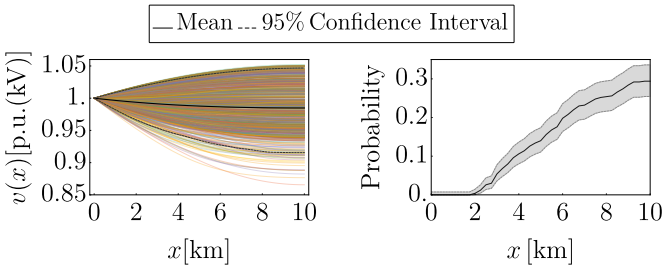


(a) Sampled cloud and injection parameters (b) Mean probability of over/under-voltage with 95% CI

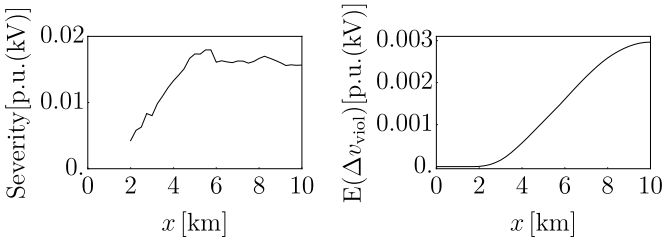


(c) Expected violation severity (d) Expected voltage limit violation

Fig. 9: Monte Carlo study of cloud-induced voltage behaviour.

$$\tilde{A}(t) = \big(A(t)\big)_+ \, \Xi\{\Upsilon(t) \le L\}\,, \Xi = \begin{cases} 1, & t \le T_L, \\ e^{-\gamma\,(t-T_L)}, & t > T_L, \end{cases}$$

Where $P_0$ is the baseline active power density profile, $\tilde{A}(t)$ is the disturbance amplitude which is non-negative, $T_L$ is the life time of the cloud, $\gamma$ is the cloud decay rate, $\Upsilon$ is the position cloud centre which is derived from a randomised speed value, and $W$ is the cloud width. This captures realistic variability in irradiance and cloud persistence. The parameters of this cloud and the DER injections ($P_0$) are sampled through Monte Carlo simulations, with each run modelling the evolution of the system over 100 min. Each Gaussian disturbance is applied to the baseline active current injections, while reactive power remains constant. To ensure statistical rigour, the number of Monte Carlo samples $N$ is determined based on a target confidence interval for violation probabilities at any time.

$$N = \frac{\kappa^2 \pi(1-\pi)}{\mu^2} = \frac{1.96^2(0.5)(1-0.5)}{0.02^2} = 2401$$

Where $\kappa$ is the z score for a 95% confidence interval, $\pi$ is the worst case violation probability, and $\mu$ is the margin of error. The probabilities of an over/under voltage event occurring at any point along the feeder can be calculated, such that $p^+(x) = \mathbb{P}[v(x) > 1.05\,\text{pu}]$, $p^-(x) = \mathbb{P}[v(x) < 0.95\,\text{pu}]$, along with 95% confidence intervals. Finally, expected violation severity and voltage violations are calculated to quantify the magnitude of potential voltage variations.

The Monte Carlo study reveals the spatial distribution of voltage risks under stochastic cloud induced variability and DER contribution. The Monte Carlo simulations Fig. 9a illustrates the diversity of voltage profiles across the sampled scenarios. This highlights the non-uniform impact of disturbances and DER output levels on the feeder. The probability of an unsafe voltage is 0 near the start of the feeder and increases asymptotically. The severity of the mean voltage violations follows the same asymptotic pattern increasing along the line. The expected violation peaks at $\approx 0.003$ pu which is significant considering the voltage limits. This probabilistic analysis helps risk assessment, identification of vulnerable points on the feeder, and determine safe limits for DER penetration.

*7) Validation against discrete method:* To verify the accuracy of the continuum formulation it is compared against a discrete MATPOWER simulation. The discrete simulation modelled the leading power factor results show in IV-A.1, this is achieved by using PQ buses with an equivalent total load and impedance along the feeder. To identify a continuum limit different numbers of buses are swept through, starting from course (10 buses) to very fine (2000 buses).

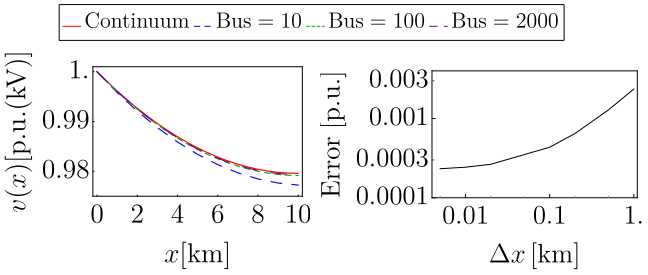


(a) Voltage magnitude (b) Log–log plot of max voltage error

Fig. 10: Discrete–continuum validation of radial feeder.

The difference of voltage outputs varies greatly when using a course discretisation but the results rapidly converge as shown in Fig. 10a. The relationship between the error and discretisation is shown in Fig. 10b, showing the error decreases approximately as a power law. These results show validate the continuum as a method to accurately predict voltages and

provides a discretisation guideline: to achieve an error below 0.02%, the feeder should be discretized with approximately one bus every 0.05% of its length.

## V. Conclusion

This paper develops a continuum model for steady-state behaviour of distribution feeders with high penetration of inverter-based resources. The resulting model describes the spatial variations of voltages through a system of differential algebraic equations utilizing a generalized injection model that incorporates constant power, current, and current density load behaviours. The continuum formulation provides a method to create accurate approximations of voltage levels, control schemes can be easily integrated, and it is capable of modelling deterministic and stochastic scenarios. These results highlight the model's potential as an alternative to detailed discrete simulations for areas of low observability and build intuition. Future work will focus on extending the model to include temporal dynamics, more complex control schemes such as coordinated controllers, and optimal DER allocation.

## VI. Appendix

TABLE III: Baseline MV feeder parameters for the continuum DAE model (pu quantities on $V_{\text{base}}$=20 kV, $S_{\text{base}}$=10 MVA).

| Symbol | Value | Units / Note |
|---|---|---|
| $V_{\text{base}}$ | 20 kV (line-to-line) | base voltage |
| $S_{\text{base}}$ | 10 MVA | base power |
| $Z_{\text{base}}$ | 40 Ω | $V_{\text{base}}^2/S_{\text{base}}$ |
| $I_{\text{base}}$ | 144.3 A | $S_{\text{base}}/(\sqrt{3}\,V_{\text{base}})$ |
| $L$ | 10 | km |
| $R$ | 0.15 | Ω/km |
| $X$ | 0.1 | Ω/km |
| $r$ | $3.75 \times 10^{-3}$ | pu/km ($R/Z_{\text{base}}$) |
| $\chi$ | $2.5 \times 10^{-3}$ | pu/km ($X/Z_{\text{base}}$) |
| $z$ | $4.501 \times 10^{-3}$ | pu/km ($\sqrt{r^2+\chi^2}$) |
| $\beta$ | 33.69° | $\arctan(\chi/r)$ |
| $P_{dP}$ | $0.137, -0.137, -0.1, 0.1, [-0.3, 0.3]$ | pu/km |
| $Q_{dP}$ | $0, P_{dP}\tan(\arccos(PF))$ | pu/km |
| | $-0.036, 0.01, 0.05$ | pu/km |
| $P^I_{\text{inj}}$ | $0, -0.0180, 0$ | pu/km |
| $Q^I_{\text{inj}}$ | $0, -0.0059, 0$ | pu/km |
| $J_{PJ}$ | 0 | pu/km |
| $J_{QJ}$ | 0 | pu/km |

*Note:* (1) Negative $P_{dP}, Q_{dP}, P^I_{\text{inj}}, Q^I_{\text{inj}}$ denote net consumption; positive denote net generation.

## References


[1] P. K. Kundu, I. M. Cohen, and D. R. Dowling, *Fluid mechanics*. Academic press, 2015.

[2] A. Semlyen, "Analysis of disturbance propagation in power systems based on a homogeneous dynamic model," *IEEE Transactions on Power Apparatus and Systems*, no. 2, pp. 676–684, 1974.

[3] ——, "Effect of nonuniformity on the continuous representation of electromechanical dynamics in large power systems," *IEEE Power Engineering Review*, vol. 18, no. 5, pp. 60–61, 2002.

[4] J. S. Thorp, C. E. Seyler, and A. G. Phadke, "Electromechanical wave propagation in large electric power systems," *IEEE Transactions on Circuits and Systems I: Fundamental Theory and Applications*, vol. 45, no. 6, pp. 614–622, 1998.

[5] M. Parashar, J. S. Thorp, and C. E. Seyler, "Continuum modeling of electromechanical dynamics in large-scale power systems," *IEEE Transactions on Circuits and Systems I: Regular Papers*, vol. 51, no. 9, pp. 1848–1858, 2004.

[6] T. Li, G. Ledwich, Y. Mishra, and J. Chow, "Power system stability implications from electromechanical wave propagation," in *IEEE PES Asia-Pacific Power and Energy Engineering Conference*, 2015, pp. 1–5.

[7] G. Tzounas, I. Dassios, and F. Milano, "Frequency divider as a continuum," *IEEE Transactions on Power Systems*, vol. 37, no. 6, pp. 4970–4973, 2022.

[8] F. M. d. S. Monteiro, J. V. de Souza, and E. N. Asada, "Analytical method to estimate the steady-state voltage impact of non-utility distributed energy resources," *Electric Power Systems Research*, vol. 218, p. 109190, 2023.

[9] L. V. Strezoski, N. R. Vojnovic, V. C. Strezoski, P. M. Vidovic, M. D. Prica, and K. A. Loparo, "Modeling challenges and potential solutions for integration of emerging ders in dms applications: power flow and short-circuit analysis," *Journal of Modern Power Systems and Clean Energy*, vol. 7, no. 6, pp. 1365–1384, 2019.

[10] G. Fusco and M. Russo, "A decentralized approach for voltage control by multiple distributed energy resources," *IEEE Transactions on Smart Grid*, vol. 12, no. 4, pp. 3115–3127, 2021.

[11] W. Zhong, G. Tzounas, and F. Milano, "Improving the power system dynamic response through a combined voltage-frequency control of distributed energy resources," *IEEE Transactions on Power Systems*, vol. 37, no. 6, pp. 4375–4384, 2022.

[12] M. Chertkov, S. Backhaus, K. Turitsyn, V. Chernyak, and V. Lebedev, "Voltage collapse and ode approach to power flows: Analysis of a feeder line with static disorder in consumption/production," *arXiv preprint arXiv:1106.5003*, 2011.

[13] D. Wang, K. Turitsyn, and M. Chertkov, "Distflow ode: Modeling, analyzing and controlling long distribution feeder," in *2012 IEEE 51st IEEE Conference on Decision and Control (CDC)*, 2012, pp. 5613–5618.

[14] ——, "DistFlow ODE: Modeling, analyzing and controlling long distribution feeder," in *IEEE Conference on Decision and Control (CDC)*. IEEE, 2012, pp. 5613–5618.

[15] N. Mizuta, Y. Susuki, Y. Ota, and A. Ishigame, "An ODE-based design of spatial charging/discharging patterns of in-vehicle batteries for provision of ancillary service," in *IEEE Conference on Control Technology and Applications*. IEEE, 2017, pp. 193–198.

[16] ——, "Synthesis of spatial charging/discharging patterns of in-vehicle batteries for provision of ancillary service and mitigation of voltage impact," *IEEE Systems Journal*, vol. 13, no. 3, pp. 3443–3453, 2019.

[17] C. Vournas, "Maximum power transfer in the presence of network resistance," *IEEE Transactions on Power Systems*, vol. 30, no. 5, pp. 2826–2827, 2014.

[18] T. Y. Na, *Computational methods in engineering boundary value problems*. Academic press, 1980, vol. 145.

[19] F. P. Beer, E. R. Johnston, J. T. DeWolf, and D. F. Mazurek, *Mechanics of Materials*, 6th ed. New York: McGraw-Hill Education, 2012, euler–Bernoulli beam equation example.